



Deposited via The University of York.

White Rose Research Online URL for this paper:

<https://eprints.whiterose.ac.uk/id/eprint/150156/>

Version: Accepted Version

---

**Article:**

Wong, Natalie Gee Kwan, Berenbeim, Jacob and Dessent, Caroline Elizabeth Helen (2019) Direct Observation of Photochemical Free Radical Production from the Sunscreen 2-Phenylbenzimidazole-5-Sulfonic Acid via Laser-Interfaced Mass Spectrometry. Chemphotochem. ISSN: 2367-0932

<https://doi.org/10.1002/cptc.201900149>

---

**Reuse**

Items deposited in White Rose Research Online are protected by copyright, with all rights reserved unless indicated otherwise. They may be downloaded and/or printed for private study, or other acts as permitted by national copyright laws. The publisher or other rights holders may allow further reproduction and re-use of the full text version. This is indicated by the licence information on the White Rose Research Online record for the item.

**Takedown**

If you consider content in White Rose Research Online to be in breach of UK law, please notify us by emailing [eprints@whiterose.ac.uk](mailto:eprints@whiterose.ac.uk) including the URL of the record and the reason for the withdrawal request.

1 **Direct Observation of Photochemical Free Radical Production from the Sunscreen 2-**  
2 **Phenylbenzimidazole-5-Sulfonic Acid via Laser-Interfaced Mass Spectrometry**

3

4 Natalie G. K. Wong, Dr. Jacob A. Berenbeim and Dr. Caroline E. H. Dessent\*

5 Department of Chemistry, University of York, Heslington, York, YO10 5DD, U.K.

6

7

8 \* Corresponding author: Email: caroline.dessent@york.ac.uk

9

10 **Abstract**

11 The common sunscreen molecule 2-phenylbenzimidazole-5-sulfonic acid (PBSA) is studied in  
12 its gas-phase deprotonated form ( $[\text{PBSA-H}]^-$ ) for the first time as an important step in achieving  
13 a better understanding of its behavior as a photosensitizer. UV laser-interfaced mass  
14 spectrometry is employed, revealing that  $[\text{PBSA-H}]^-$  photofragments into three ionic products  
15 ( $m/z$  208, 193, and 80) with distinctive wavelength-dependent production profiles. Both the  
16  $m/z$  208 and 80 channels produce associated neutral free radical species. Collision-induced  
17 dissociation is performed on  $[\text{PBSA-H}]^-$ , showing that its hot ground-state dissociates only into  
18  $m/z$  193 (statistical fragment). Therefore, the  $m/z$  208 and 80 fragments which are produced  
19 strongly through the UVA/UVB are characterized as non-statistical photofragments associated  
20 with non-ergodic excited-state decay. Our observation of non-statistical photofragments reveal  
21 that  $[\text{PBSA-H}]^-$  is not behaving as a model sunscreen molecule. Further, our results indicate  
22 that the  $T_1$  state, associated with photosensitization, decays with direct free radical production.

23

24 **Keywords**

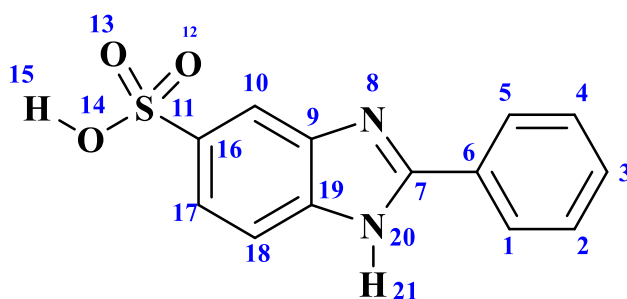
25 Sunscreen, free radicals, laser spectroscopy, photolysis, photosensitizer.

26

27

## 28 1. Introduction

29 Sunscreens are widely employed to protect human skin from sunburn and the long-term  
30 consequences of exposure to the sun. The suitability of a given sunscreen molecule depends  
31 on a range of factors, but its effectiveness will clearly be limited if it behaves as a  
32 photosensitizer.<sup>[1,2]</sup> (A photosensitizer is a molecule that subsequent to its activation by light,  
33 produces a chemical change in another molecule. Commonly, this involves generating reactive  
34 oxygen species that initiate further chemical reactions.) Surprisingly, several common organic  
35 sunscreen molecules (*e.g.* octocrylene, octylmethoxycinnamate, or oxybenzone) have been  
36 reported to enhance the production of reactive oxygen species.<sup>[3-8]</sup> 2-phenylbenzimidazole-5-  
37 sulfonic acid (PBSA) is one such widely-used sunscreen (Scheme 1), which has been found to  
38 photogenerate reactive oxygen species and oxidize guanine residues *in cellulo* under UV  
39 radiation.<sup>[9-11]</sup> There is currently a need to better understand the photosensitization mechanisms  
40 that occur for UV filters such as PBSA, in order to aid the rational development of future  
41 sunscreens.<sup>[1,2]</sup>



42

43 **Scheme 1.** Schematic diagram of PBSA with atom labels.

44 In this paper, we adopt a new approach to better understand the photodegradation pathways  
45 and hence photosensitization mechanisms that are available to PBSA through applying the  
46 novel technique of laser-interfaced photodissociation mass spectrometry.<sup>[12-14]</sup> PBSA exists as  
47 a deprotonated species, *i.e.* [PBSA-H]<sup>-</sup>, in solution due to the low pK<sub>a</sub> of its sulfonic acid group.  
48 Here, we employ electrospray ionization to transfer [PBSA-H]<sup>-</sup> from solution into the gas phase  
49 where the ion is then mass selected and interrogated with laser photons over a wide UV range.  
50 This allows us to monitor how the absorbance of the anion varies with wavelength, while  
51 simultaneously measuring the production of any photoproducts.<sup>[12,13]</sup> Our laser-based approach  
52 is in the spirit of a number of recent studies where advanced spectroscopic techniques have  
53 been applied to sunscreen molecules under highly-controlled conditions.<sup>[15-23]</sup>

54 Recent computational studies by Zhang *et al.* and Shen have been performed on PBSA to better  
55 understand its photophysical properties.<sup>[24,25]</sup> Zhang *et al.* used density functional theory to  
56 assess the potential for triplet-state electron transfer from different protonation states of PBSA  
57 to triplet oxygen.<sup>[24]</sup> They found that deprotonated PBSA could spontaneously transfer an  
58 electron to  $^3\text{O}_2$  to generate reactive  $\text{O}_2^-$ , with the different protonation states varying in their  
59 propensity to effect electron transfer. Shen used time-dependent density functional theory to  
60 assess PBSA's photosensitizing potential, finding further evidence that singlet oxygen can be  
61 produced from the triplet excited state.<sup>[25]</sup> To date, no computational studies have been  
62 performed to calculate the excited-state potential energy surfaces or direct photodegradation  
63 products. There have also been a number of solution-phase photochemical studies of PBSA,  
64 which have confirmed that the  $T_1$  state can generate reactive oxygen species, and that their  
65 production is pH dependent.<sup>[10,26-30]</sup> Experiments to track direct photodegradation products in  
66 solution are challenging due to secondary reactions and environmental effects. However, such  
67 measurements are important outside of the immediate interest in sunscreens, since these  
68 molecules are common aquatic pollutants, and a full understanding of potential photoproducts  
69 and their toxicity is crucial.<sup>[26-30]</sup>

70 Gas-phase photochemical studies provide a complementary approach to mapping  
71 photodegradation where photoproducts can be directly identified, and experimental results can  
72 be straightforwardly compared to theoretical calculations. However, gas-phase laser  
73 spectroscopy of the ionic forms of sunscreen molecules are currently sparse,<sup>[12,15]</sup> with only  
74 oxybenzone having been studied very recently in its protonated and deprotonated forms.<sup>[15]</sup>  
75 Notably, deprotonated oxybenzone was observed to photofragment with production of methyl  
76 radicals in the UVB. This result is concerning as it adds to long-standing concerns that some  
77 sunscreens can produce free radicals following photoexcitation.<sup>[19]</sup> In the current study on  
78 PBSA, we aim to better understand the generality of our recent oxybenzone results, as well as  
79 providing a more detailed insight into the photosensitizing behavior of PBSA.

80

## 81 **Experimental and Computational Details**

82 The gaseous ion absorption (photodepletion) and photofragment production spectra of [PBSA-  
83 H]<sup>+</sup>, were recorded *in vacuo* using action spectroscopy. An AmaZon SL mass spectrometer  
84 (Bruker Daltonics Inc., Billerica, MA, USA) modified for laser-interfaced mass spectrometry  
85 (LIMS), was used as described previously.<sup>[12,13]</sup> PBSA was purchased from Sigma-Aldrich

86 (St. Louis, MA, USA) and used as received. HPLC-grade acetonitrile was purchased from  
87 Fisher Scientific, Inc. (Pittsburgh, PA, USA). PBSA solutions ( $1 \times 10^{-5}$  mol dm<sup>-3</sup> in CH<sub>3</sub>CN)  
88 were electrosprayed at a capillary temperature 160 °C.

89 [PBSA-H]<sup>-</sup> was mass selected (m/z 273) and isolated in the ion trap prior to laser irradiation.  
90 Photons were produced by an Nd:YAG pumped OPO laser (Surelite™/Horizon™, Amplitude  
91 Laser Group, San Jose, CA, USA), giving  $0.3 \pm 10\%$  mJ across the range 500-216 nm (2.48-  
92 5.74 eV), with 2 nm laser step sizes. Photofragmentation experiments were conducted with an  
93 ion accumulation time of 10 ms. To minimize the possibility of multiphoton events via  
94 sequential absorption, each mass-selected ion packet interacts with only one laser pulse  
95 (fragmentation time of 100 ms), and photodepletion restricted to ~40% of the precursor ion at  
96 the wavelength of maximum absorption. Multiphoton events via instantaneous absorption of  
97 multiple photons in the Frank-Condon region are negligible as the laser beam is only softly  
98 focused through the ion-trap region. Photodepletion (PD) of [PBSA-H]<sup>-</sup> was measured as a  
99 function of the scanned wavelength, with photofragment production (PF) recorded  
100 simultaneously:

$$101 \quad \text{Photodepletion Intensity} = \frac{\ln\left(\frac{\text{Int}_{\text{OFF}}}{\text{Int}_{\text{ON}}}\right)}{\lambda \times P} \quad [1a]$$

$$102 \quad \text{Photofragmentation Intensity} = \frac{\left(\frac{\text{Int}_{\text{FRAG}}}{\text{Int}_{\text{OFF}}}\right)}{\lambda \times P} \quad [1b]$$

$$103 \quad \text{Relative Ion Yield} = \text{Int}_{\text{FRAG}} / \text{Int}_{\text{PFT}} \quad [1c]$$

104 In these expressions, Int<sub>OFF</sub> and Int<sub>ON</sub> are the laser off and on parent ion peak intensities  
105 respectively; Int<sub>FRAG</sub> is the fragment intensity with the laser on;  $\lambda$  is the excitation wavelength  
106 (nm); P is the laser pulse energy (mJ); and Int<sub>PFT</sub> is the sum of the photofragment ion intensities  
107 with the laser on. The photodepletion spectrum is considered to be equivalent to the gaseous  
108 absorption spectrum in the limit where excited state fluorescence is negligible.<sup>[13,14,31]</sup>  
109 Photodepletion intensities were taken from an average of three runs at each wavelength of the  
110 range studied. We note that fragment ions with m/z < 50 are not detectable in our mass  
111 spectrometer since low masses fall outside the ion-trap mass-window.

112 Higher-energy collisional dissociation (HCD) was performed to investigate the ground-state  
113 thermal fragmentation characteristics of [PBSA-H]<sup>-</sup>, using an Orbitrap™ Fusion Tribrid mass  
114 spectrometer (Thermo Fisher Scientific, Waltham, MA, U.S.A.) as described previously.<sup>[32,33]</sup>  
115 Solution-phase UV-VIS absorption spectra of PBSA (aqueous solution;  $3 \times 10^{-5}$  mol dm<sup>-3</sup>)

116 were recorded with a UV-1800 spectrophotometer (Shimadzu, Kyoto, Japan) with a 10 mm  
117 UV quartz cuvette, with deionized H<sub>2</sub>O as the baseline solvent.

118 All calculations were performed using Density Functional Theory (DFT) at the B3LYP/6-  
119 31+G\*\* level in Gaussian 09.<sup>[34]</sup> The bulk solvent effect of CH<sub>3</sub>CN was considered by using  
120 the integral equation formalism polarized continuum model (IEFPCM) based on the self-  
121 consistent-reaction-field (SCRF) method. All reported structures correspond to true minima, as  
122 confirmed by frequency calculations.

123

## 124 **2. Results and Discussion**

### 125 **2.1 Identification of the Deprotonation Site in [PBSA-H]<sup>-</sup> via Density Functional Theory** 126 **Calculations**

127 The sulfonic acid group is a strongly acidic group, so PBSA will be deprotonated at the **H15**  
128 position (Scheme 1) in aqueous solution to form the sulfonate monoanion.<sup>[29]</sup> Deprotonation  
129 is also possible from the **H21** position at higher pH.<sup>[29]</sup> Relative energies of the two  
130 deprotomers of [PBSA-H]<sup>-</sup> were calculated in the gas phase and in acetonitrile to reveal which  
131 deprotomer or deprotomer(s) will be produced following electrospray (Table 1). (Electrospray  
132 does not always transfer the most stable solution-phase ion to the gas phase).<sup>[12,35,36]</sup> In the  
133 subsequent discussion, we label the two possible deprotomers as **O14** and **N20** in line with the  
134 excess negative-charge site.

135 As expected, deprotonation is favored from the sulfonic acid group (**O14**), both in the gas phase  
136 and in acetonitrile, although the relative energies of the two deprotomers are closer in the gas  
137 phase. Boltzmann population calculations indicate that the **O14** deprotomer dominates  
138 (>99.9%) in acetonitrile at 458 K. Since electrospray from acetonitrile solutions maintains the  
139 solution-phase ratios of different tautomeric species,<sup>[12,35]</sup> we expect the **O14** deprotomer to  
140 almost entirely dominate the gaseous ion population. Vertical detachment energies (VDE) of  
141 the gaseous deprotomers are also listed in Table 1.

142

### 143 **2.2 UV Absorption Spectra of [PBSA-H]<sup>-</sup>: Gas Phase versus Solution Phase**

144 Figure 1 shows the electrospray ionization mass spectrum obtained when a solution of PBSA  
145 in acetonitrile is sprayed in negative ion mode, showing [PBSA-H]<sup>-</sup> (m/z 273) as the dominant

146 peak. The gas-phase absorption spectrum of mass-selected [PBSA-H]<sup>-</sup> across the 2.48-5.74 eV  
147 (500-216 nm) range, recorded *via* photodepletion, is shown in Figure 2a. Mass selection is a  
148 key advantage of the experimental approach we employ here as it allows us to directly probe  
149 the intrinsic properties of the [PBSA-H]<sup>-</sup> anion.

150 The gaseous absorption spectrum of [PBSA-H]<sup>-</sup> displays strong absorption in the UVA region  
151 (with an absorption onset around 3.40 eV) through a band which then reduces in intensity  
152 through the UVB range. Absorption again increases to higher energies through the UVC  
153 region. To aid discussion of the photofragment production spectra (see Section 2.3), the  
154 photodepletion spectrum has been labelled as being composed of features **I-IV**, with **I**  
155 representing the strong UVA-UVB band. Figure 2b presents an aqueous absorption spectrum  
156 of PBSA (pH 7.1) obtained as part of this work for direct comparison with the gas-phase  
157 absorption spectrum. The spectrum agrees well with previously-published ones.<sup>[5,11,26-29]</sup>  
158 Comparing the gaseous and solution-phase spectra, feature **I** can be seen to blue-shift  
159 significantly on going from the gas-phase to solution (band maxima at ~340 nm versus 315  
160 nm), a trend which is consistent with the transition displaying charge-transfer character where  
161 the excess charge is more localized in the initial ion than in the excited state.<sup>[37]</sup>

162 Given that the calculated VDE of the **O14** deprotomer is 4.39 eV, we predict that band **I** exists  
163 within the bound (non-electron-detached) region for this anionic species. Electronic excitations  
164 lying above this energy occur within the electron detachment continuum, so that any gas-phase  
165 photoexcitation above 4.39 eV is likely to be accompanied by electron detachment.<sup>[38]</sup>

166

### 167 **2.3 Photofragmentation of [PBSA-H]<sup>-</sup>**

168 We next turn to exploring the photofragment ions that are associated with the excited states  
169 evident in the Figure 2a spectrum. Figure 3 displays the difference (laser on - laser off)  
170 photofragment mass spectra of [PBSA-H]<sup>-</sup> irradiated at the photoabsorption maxima of features  
171 **I-IV** (3.8, 4.5, 4.9, and 5.3 eV, respectively). Photofragmentation produces m/z 80, 193, and  
172 208 as the dominant ionic products, with equations [2a]-[2c] illustrating the fragmentation  
173 pathways associated with their production:



176  $\rightarrow$  m/z 208 + HSO<sub>2</sub><sup>•</sup> [2c]

177 Table 2 lists the proposed structures of the ionic photofragments and their accompanying  
178 neutral fragments. Inspection of the structures shown in Table 2 reveals that  
179 photofragmentation is localized around the **S11-C16** bond, with pathways [2a] and [2b] arising  
180 from the fission of this bond with the excess charge moving in two different directions.  
181 Photofragment m/z 208 is produced *via* a less direct pathway, which involves intramolecular  
182 rearrangement to eject the HSO<sub>2</sub><sup>•</sup> neutral. We note that the structures of the lower mass  
183 fragments mean that these ions cannot be produced through fragmentation of higher mass ions,  
184 ruling out the possibility that they are produced through a sequential multiphoton processes.  
185 The key point of note about the photofragment pathways, is that two of these pathways ([2a]  
186 and [2c]) result in the production of free-radical species.

187 To provide further insight into the nature of the [PBSA-H]<sup>-</sup> excited states and decay pathways,  
188 Figures 4b-4d present the production spectra for the three ionic photofragments m/z 80, 193,  
189 and 208, with the parent [PBSA-H]<sup>-</sup> photodepletion spectrum displayed again in Figure 4a for  
190 ease of comparison. The photofragment production spectra highlight that all of the  
191 photofragments are produced to some extent across the entire photoexcitation range from 3.40-  
192 5.74 eV.

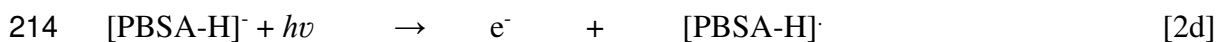
193 The action spectrum of the lowest mass ionic photofragment, m/z 80, is shown in Figure 4b  
194 and is very similar to the [PBSA-H]<sup>-</sup> gaseous absorption spectrum. This is also largely true for  
195 the m/z 208 photofragment (Figure 4d), although this photofragment is produced more weakly  
196 across the high-energy **III/IV** regions. The profile of the high-energy spectral range for the m/z  
197 208 photofragment is similar to other photofragment spectra we have recorded previously,  
198 where a higher-mass photofragment dissociates into a lower-mass photofragment at high  
199 internal excitation energy.<sup>[12]</sup>

200 Figure 4c displays the photoproduction spectrum of the most intense ionic photofragment  
201 (m/z 193), which is notable compared to the other two photofragments as it is produced much  
202 less strongly through region **I**, with intensity subsequently increasing with excitation  
203 wavelength into the UVC region.

204 It is evident from the data presented in Figures 3 and 4 that the relative production of the three  
205 observed photofragments from [PSBA-H]<sup>-</sup> varies significantly as a function of photon energy.  
206 Figure 5 presents a plot of the relative ion yield of the photofragments, providing a concise  
207 overview of photofragment production. Within the UVA region (3.5-4.1 eV), the relative ion

208 yields of the m/z 80 and 208 photofragments are larger than that of the m/z 193 ion. At photon  
209 energies above 4.1 eV, however, production of the m/z 193 fragment increases strongly, with  
210 relative production peaking around 4.5 eV. These results are discussed in the context of  
211 PBSA's ability to act as an efficient UV filter in the next section.

212 Electron loss is a dominant photofragmentation channel for [PBSA-H]<sup>-</sup> as for other gaseous  
213 anions we have studied,<sup>[15, 38]</sup> *i.e.*



215 Section S2 of the Supporting Information provides an electron detachment yield spectrum, and  
216 further details of the extent of electron detachment versus ionic fragmentation. At 224 nm, for  
217 example, electron detachment is estimated to constitute 85% of photodepletion compared to  
218 15% branching into ionic fragments. Despite the strong propensity for electron detachment in the  
219 gas-phase, it is well established that the propensity of an anionic molecule to photodetach will be  
220 quenched upon solvation,<sup>[39]</sup> so simple electron detachment is likely to be a less important channel  
221 compared to ionic fragmentation in solution.

222

## 223 **2.4 Thermal Fragmentation versus Photofragmentation**

224 To act as an efficient sunscreen, a molecule must be able to convert the harmful UV radiation  
225 it has absorbed into benign thermal energy. This is achieved by the electronic excited state(s)  
226 being able to rapidly relax back to the electronic ground state from where excess energy is  
227 dissipated by heat loss.<sup>[1,2]</sup> In solution, this thermal energy can be lost to the bulk solvent *via*  
228 vibrational relaxation, but in the gas phase, this energy is conserved within the molecular  
229 system and the ensuing hot ground state will dissociate across the available fragmentation  
230 barriers which are the same as those that are available to the isolated molecule when it is heated  
231 (so called "statistical fragmentation"). For molecular ions, a closely comparable "heating"  
232 process occurs in collision-induced dissociation.<sup>[40]</sup> [PBSA-H]<sup>-</sup> was therefore subjected to  
233 collisional excitation to allow the fragmentation pathways associated with hot ground-state  
234 fragmentation to be identified.

235 Figure 6 displays the higher-energy collisional dissociation (HCD) fragmentation curves for  
236 [PBSA-H]<sup>-</sup>. Collisional activation reveals that the m/z 193 molecular ion completely  
237 dominates the thermal fragmentation profile of [PBSA-H]<sup>-</sup>, with the m/z 80 and 208 fragments  
238 only being seen as extremely minor fragments at the very highest collisional energies

239 (>50%).<sup>[41]</sup> We can therefore conclude that statistical fragmentation of [PBSA-H]<sup>-</sup> would  
240 proceed with production of only the m/z 193 fragment (pathway [2b]).

241 The relative ion yield plots shown in Figure 5 are clearly not consistent with a picture where  
242 UVA/UVB excitation of isolated [PBSA-H]<sup>-</sup> leads to the ultrafast decay back to the electronic  
243 ground state, followed by statistical fragmentation solely into the m/z 193 fragment. (If this  
244 was the case, we would expect to see m/z 193 as the only photofragment with an ion yield  
245 profile that follows the absorption spectrum.) Instead, photoexcitation across the UV leads to  
246 strong production of the non-statistical fragments (m/z 80 and 208). Such non-statistical (or  
247 non-ergodic) processes occur when dissociation proceeds directly from the excited state  
248 without significant adiabatic conical-intersection involvement to return the system back to the  
249 ground state in the vicinity of the initial geometry.<sup>[42]</sup> This is particularly true in the UVA region  
250 where the m/z 193 fragment is the minor fragment, indicating non-statistical excited state decay  
251 dominates.

252 The ion-yield plots displayed in Figure 5 show that statistical dissociation, i.e. dissociation into  
253 m/z 193, is enhanced in the UVC region < 280 nm. For deprotonated PBSA as well as neutral  
254 PBSA, there are currently no calculations of the excited state potential energy surfaces, so the  
255 molecular mechanism that precedes statistical decay is currently unknown. From precedents in  
256 other organic molecular systems, it is likely that this could be mediated by a conical intersection  
257 involving a bond rotation of the bridging C-C linking the imidazole and benzene,<sup>[43]</sup> although  
258 it is also possible a conical intersection could be reached may be rotation of the sulfonate group  
259 to the imidazole instead. Calculations of the excited state surfaces are highly desirable to  
260 provide further insight into the mechanism(s) involved.<sup>[43]</sup>

261

## 262 **2.5 Implications of the Gas-Phase Results for Solution-Phase Photochemistry**

263 The most detailed solution-phase study of PBSA photochemistry and photophysics conducted  
264 to date was that of Inbaraj et al.<sup>[10]</sup> Measurements included the determination of the UVB  
265 quantum yield for production of singlet oxygen from deprotonated PBSA (0.05 in D<sub>2</sub>O), as  
266 well as the fluorescence quantum yield (0.63). They noted that phosphorescence was also  
267 detected, although no quantum yield for this channel was reported. Importantly, the T<sub>1</sub> triplet  
268 excited state was found to be sufficiently long-lived at 77K for the characteristic electron  
269 paramagnetic resonance half-field transition to be detectable. No photofragmentation quantum  
270 yields were reported in the study.

271 It is important at this point to consider how our gas-phase results relate to the photochemistry  
272 of PBSA in solution. In Section 2.2, we noted that the region **I** absorption blue-shifts upon  
273 solvation. It is reasonable to assume that the photochemistry we observe across region **I** in the  
274 gas-phase (3.4-4.2 eV), similarly blue-shifts in solution to the 3.8-4.6 eV range. Zhang *et al.*  
275 has calculated the solution-phase S<sub>1</sub> excitation energy of [PBSA-H]<sup>-</sup> as 4.045 eV,<sup>[24]</sup> an energy  
276 which lies in region **I** (solvated). By analogy, we expect that the S<sub>1</sub> state is reached through  
277 gas-phase region **I** in our experiment. This state is important as it is believed to act as a  
278 doorway to the long-lived T<sub>1</sub> state.<sup>[24]</sup> It is notable that the strong production of non-statistical  
279 photofragments associated with pathways [2a] and [2c] occurs through region **I**, leading us to  
280 conclude that these are the direct photodegradation products of the T<sub>1</sub> state.<sup>[24,25,29]</sup> Similarly,  
281 since the T<sub>1</sub> state has been previously attributed with leading to PBSA's behavior as a  
282 photosensitizer,<sup>[24,25,29]</sup> our results suggest that photosensitization by PBSA in solution is not  
283 simply associated with electron and energy transfer from the T<sub>1</sub> state, but also through direct  
284 formation of free radical products. We note that geminate recombination of any free radical  
285 photoproducts may occur in solution, and it will be important in future solution-phase  
286 measurements to directly explore whether these direct free radical products can be detected,  
287 for example by employing techniques such as spin trapping.<sup>[44]</sup>

288

### 289 **3. Concluding Remarks**

290 In summary, we report for the first time the gaseous electronic photoabsorption spectrum and  
291 direct photofragment production profile spectra of the native form of PBSA, a popular FDA-  
292 approved UV filter found within many existing commercial sunscreens. The novelty of our  
293 gas-phase experiment is that it allows us to map the direct laser-induced photodegradation  
294 products of [PBSA-H]<sup>-</sup>, away from the complications of bulk mixtures where secondary  
295 photoproducts can dominate. Strikingly, we observe evidence<sup>[44]</sup> for high-yield production of  
296 free-radical species at photon energies between 3.5-5.5 eV. [PBSA-H]<sup>-</sup> is observed to largely  
297 photodissociate primarily *via* the heterolytic cleavage of the **S11-C13** bond (pathway [2b]);  
298 however, competitive homolytic dissociation yielding odd-electron products (pathways [2a]  
299 and [2c]) is seen strongly across UVA/UVB absorbance wavelengths. By comparing our  
300 gaseous spectra with the solution-phase absorption spectrum, we conclude that the non-  
301 statistical odd-electron photofragments (pathways [2a] and [2c]) are the direct  
302 photodegradation products of the T<sub>1</sub> state. Indeed, the long-range repulsive interaction inherent

303 in the triplet state is known to aid in the breakdown of such states into such free radical pairs.<sup>[45]</sup>  
304 The identification of the direct photoproducts in this work is important as it can guide detection  
305 of the direct photolysis products in future condensed-phase studies, as well as informing  
306 assessment of the possible toxicity of photoproducts. Furthermore, our results indicate that  
307 future theoretical studies (which are generally performed on gaseous molecules initially)  
308 should include this direct photodegradation pathway to provide a more complete understanding  
309 of the photosensitizing behavior of PBSA. Such work is highly desirable to guide the rational  
310 development of improved UV filters.<sup>[43,46]</sup>

311

### 312 **Acknowledgements**

313 This work was funded through the Leverhulme Trust Research Project Grant RPG-2017-147.  
314 We thank the University of York and the Department of Chemistry for provision of funds for  
315 the OPO laser system. We are grateful for computational support from the University of York  
316 High Performance Computing service, Viking and the Research Computing team. The York  
317 Centre of Excellence in Mass Spectrometry, used for the higher-energy collisional dissociation  
318 (HCD) work, was created thanks to a major capital investment through Science City York,  
319 supported by Yorkshire Forward with funds from the Northern Way Initiative, and  
320 subsequently received additional support from the EPSRC. We also thank Mathew Hawkrige  
321 for early contributions to this work.

322

### 323 **Conflict of Interest**

324 The authors declare no conflict of interest.

325

326

327 **References**

- 328 [1] S. Forestier, *J. Am. Acad. Dermatol.* **2008**, *58*, S133-8.
- 329 [2] F. Gasparro, *Sunscreen Photobiology*, Springer, Berlin, **1997**.
- 330 [3] K. M. Hanson, E. Gratton, C. J. Bardeen, *Free Radic. Biol. Med.* **2006**, *41*, 1205–
- 331 1212.
- 332 [4] V. Brezová, S. Gabčová, D. Dvoranová, A. Staško, *J. Photochem. Photobiol. B Biol.*
- 333 **2005**, *79*, 121–134.
- 334 [5] N. Serpone, A. Salinaro, A. V. Emeline, S. Horikoshi, H. Hidaka, J. Zhao,
- 335 *Photochem. Photobiol. Sci.* **2002**, *1*, 970–981.
- 336 [6] P. J. McHugh, J. Knowland, *Photochem. Photobiol.* **1997**, *66*, 276–81.
- 337 [7] J. M. Allen, C. J. Gossett, S. K. Allen, *Chem. Res. Toxicol.* **1996**, *9*, 605–609.
- 338 [8] J. Knowland, E. A. McKenzie, P. J. McHugh, N. A. Cridland, *FEBS Lett.* **1993**, *324*,
- 339 309–313.
- 340 [9] N. Bastien, J.-F. Millau, M. Rouabhia, R. J. H. Davies, R. Drouin, *J. Invest. Dermatol.*
- 341 **2010**, *130*, 2463–2471.
- 342 [10] J. J. Inbaraj, P. Bilski, C. F. Chignell, *Photochem. Photobiol.* **2002**, *75*, 107–16.
- 343 [11] C. Stevenson, R. J. H. Davies, *Chem. Res. Toxicol.* **1999**, *12*, 38–45.
- 344 [12] E. Matthews, C. E. H. Dessent, *Phys. Chem. Chem. Phys.* **2017**, *19*, 17434–17440.
- 345 [13] E. Matthews, A. Sen, N. Yoshikawa, E. Bergström, C. E. H. Dessent, *Phys. Chem.*
- 346 *Chem. Phys.* **2016**, *18*, 15143–15152.
- 347 [14] R. Antoine and P. Dugourd, *Phys. Chem. Chem. Phys.* **2011**, *13*, 16494–16509.
- 348 [15] N. G. K. Wong, J. A. Berenbeim, M. Hawkrigde, E. Matthews, C. E. H. Dessent,
- 349 *Phys. Chem. Chem. Phys.* **2019**, *21*, 14311-14321.
- 350 [16] N. D. N. Rodrigues, N. C. Cole-Filipiak, M. A. P. Turner, K. Krokidi, G. L. Thornton,
- 351 G. W. Richings, N. D. M. Hine, V. G. Stavros, *Chem. Phys.* **2018**, *515*, 596–602.
- 352 [17] L. A. Baker, M. Staniforth, A. L. Flourat, F. Allais, V. G. Stavros, *ChemPhotoChem*
- 353 **2018**, *2*, 743–748.
- 354 [18] C. Ma, C. T. L. Chan, R. C. T. Chan, A. K. W. Wong, B. P. Y. Chung, W. M. Kwok,
- 355 *Phys. Chem. Chem. Phys.* **2018**, *20*, 24796–24806.
- 356 [19] M. T. Ignasiak, C. Houee-Levin, G. Kciuk, B. Marciniak, T. Pedzinski, C. Houée-
- 357 Levin, G. Kciuk, B. Marciniak, T. Pedzinski, *ChemPhysChem* **2015**, *16*, 628–633.
- 358 [20] S. Wang, S. Schatz, M. C. Stuhldreier, H. Böhnke, J. Wiese, C. Schröder, T. Raeker,
- 359 B. Hartke, J. K. Keppler, K. Schwarz, et al., *Phys. Chem. Chem. Phys.* **2017**, *19*,
- 360 30683–30694.

- 361 [21] E. M. M. Tan, M. Hilbers, W. J. Buma, *J. Phys. Chem. Lett.* **2014**, *5*, 2464–2468.
- 362 [22] J. C. Dean, R. Kusaka, P. S. Walsh, F. Allais, T. S. Zwier, *J. Am. Chem. Soc.* **2014**,  
363 *136*, 14780–14795.
- 364 [23] M.-O. Winghart, J.-P. Yang, M. Kuhn, A.-N. Unterreiner, T. J. A. Wolf, P. D. Dau,  
365 H.-T. Liu, D.-L. Huang, W. Klopper, L.-S. Wang and M. M. Kappes, *Phys. Chem.*  
366 *Chem. Phys.* **2013**, *15*, 6726–6736.
- 367 [24] S. Zhang, J. Chen, X. Qiao, L. Ge, X. Cai, G. Na, *Environ. Sci. Technol.* **2010**, *44*,  
368 7484–7490.
- 369 [25] L. Shen, *Spectrochim. Acta - Part A Mol. Biomol. Spectrosc.* **2015**, *150*, 187–189.
- 370 [26] W. H. M. Abdelraheem, X. He, Z. R. Komy, N. M. Ismail, D. D. Dionysiou, *Chem.*  
371 *Eng. J.* **2016**, *288*, 824–833.
- 372 [27] Y. Ji, Photochemical and photocatalytic degradation of pharmaceutical and personal  
373 care products (PPCPS) in aqueous solution: a case study of atenolol and 2-  
374 phenylbenzimidazole-5-sulfonic acid, Ph.D., Université Claude Bernard - Lyon I,  
375 **2014**.
- 376 [28] Y. Ji, L. Zhou, C. Ferronato, A. Salvador, X. Yang, J.-M. Chovelon, *Appl. Catal. B*  
377 *Environ.* **2013**, *140–141*, 457–467.
- 378 [29] Y. Ji, L. Zhou, Y. Zhang, C. Ferronato, M. Brigante, G. Mailhot, X. Yang, J.-M.  
379 Chovelon, *Water Res.* **2013**, *47*, 5865–5875.
- 380 [30] E. De Laurentiis, M. Minella, M. Sarakha, A. Marrese, C. Minero, G. Mailhot, M.  
381 Brigante, D. Vione, *Water Res.* **2013**, *47*, 5943–5953.
- 382 [31] S. K. Sagoo, R. A. Jockusch, *J. Photochem. Photobiol. A Chem.* **2011**, *220*, 173–178.
- 383 [32] R. Cercola, E. Matthews, C. E. H. Dessent, *J. Phys. Chem. B* **2017**, *121*, 5553–5561.
- 384 [33] J. V Olsen, B. Macek, O. Lange, A. Makarov, S. Horning, M. Mann, *Nat. Methods*  
385 **2007**, *4*, 709–712.
- 386 [34] M. J. Frisch, G. W. Trucks, H. B. Schlegel, G. E. Scuseria, M. A. Robb, J. R.  
387 Cheeseman, G. Scalmani, V. Barone, B. Mennucci, G. A. Petersson, et al., *Gaussian*  
388 *09, Rev. D.01*, Gaussian Inc. **2009**, Wallingford, CT.
- 389 [35] D. Schröder, M. Buděšínský, J. Roithová, *J. Am. Chem. Soc.* **2012**, *134*, 15897–  
390 15905.
- 391 [36] E. Matthews, C. E. H. Dessent, *J. Phys. Chem. A*, **2016**, *120*, 9209–9216.
- 392 [37] S. B. Nielsen, M. B. Nielsen, A. Rubio, *Acc. Chem. Res.* **2014**, *47*, 1417–1425.
- 393 [38] A. Henley, H. H. Fielding, *Int. Rev. Phys. Chem.* **2019**, *38*, 1–34.

- 394 [39] D. Serxner, C. E. H. Dessent, M. A. Johnson, *J. Chem. Phys.* **1996**, *105*, 7231-7234.
- 395 [40] P. B. Armentrout, *J. Am. Soc. Mass Spectrom.* **2002**, *13*, 419–434.
- 396 [41] Whilst we have not quantitatively calibrated the HCD collision energies used in this  
397 experiment, earlier work from our group has established that the 20-38% HCD collision  
398 energy range closely correlates to internal energies of ~4-6 eV,<sup>[32]</sup> which falls directly  
399 into the range of photon energies used within this experiment.
- 400 [42] B. Lucas, M. Barat, J. A. Fayeton, C. Jouvét, P. Çarçabal, G. Grégoire, *Chem. Phys.*  
401 **2008**, *347*, 324–330.
- 402 [43] L. A. Baker, B. Marchetti, T. N. V. Karsili, V. G. Stavros, M. N. R. Ashfold, *Chem.*  
403 *Soc. Rev.* **2017**, *46*, 3770–3791.
- 404 [44] A. Alberti, D. Macciantelli, *Spin Trapping. Electron Paramagnetic Resonance*: John  
405 Wiley & Sons, Inc.; **2008**, 285–324.
- 406 [45] B. Marchetti, T. N. V. Karsili, M. N. R. Ashfold, *Phys. Chem. Chem. Phys.* **2019**, *21*,  
407 14418-14428.
- 408 [46] R. Losantos, I. Funes-Ardoiz, J. Aguilera, E. Herrera-Ceballos, C. García-Iriepa, P.  
409 Campos, D. Sampedro, *Angew. Chem. Int. Ed.* **2017**, *56*, 2632-2635.
- 410
- 411

412 **TABLES**

413

414 **Table 1.** Calculated relative electronic energies and gaseous vertical detachment energies  
 415 (VDE) of the deprotonated isomers of PBSA calculated at the B3LYP/6-31+G\*\* level.

Isomer	Relative Electronic Energy (kJ/mol) <sup>[a]</sup>		VDE (eV) <sup>[b]</sup>
	Gaseous	Acetonitrile	
<b>O14</b>	0	0	4.39
<b>N20</b>	14.3	90.7	4.04

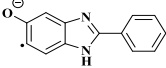
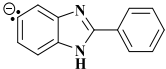
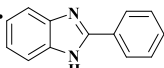
416 <sup>[a]</sup> Zero-point energy corrected.

417 <sup>[b]</sup> VDE =  $E$  (neutral at optimized anion geometry) –  $E$  (anion). This is included in the table  
 418 for comparison with the experimental spectra.

419

420

421 **Table 2.** Proposed structures for the ionic fragments of deprotonated PBSA ( $m/z$  273)  
 422 produced upon higher-energy collisional dissociation (HCD) and laser photoexcitation.

Ionic Fragment Mass ( $m/z$ ) <sup>[a]</sup>	Proposed Structure of Fragment	Accompanying Neutral Fragment Lost	Observed in HCD <sup>[b]</sup>	Observed in Laser Photoexcitation <sup>[b]</sup>
208		HSO <sub>2</sub> •	✓ (vw)	✓ (w)
193		SO <sub>3</sub>	✓ (vs)	✓ (s)
80	SO <sub>3</sub> <sup>•-</sup>		✓ (vw)	✓ (m)

423 <sup>[a]</sup> Determined with mass accuracy > 0.3 amu.424 <sup>[b]</sup> Very strong (vs), strong (s), medium (m), weak (w), and very weak (vw).

425

426

427

428 **FIGURE CAPTIONS**

429 **Scheme 1.** Schematic diagram of PBSA with atom labels.

430 **Figure 1.** Negative ion electrospray ionization mass spectrum of [PBSA-H]<sup>-</sup> (m/z 273).

431 **Figure 2. (a)** Gas-phase UV absorption (photodepletion) spectrum of [PBSA-H]<sup>-</sup>. **(b)** Aqueous  
432 UV absorption spectrum of PBSA ( $3 \times 10^{-5}$  mol dm<sup>-3</sup>) at pH 7.1.

433 **Figure 3.** Photofragment difference (laser on – laser off) mass spectra of [PBSA-H]<sup>-</sup>, excited  
434 at four photodepletion maxima of **(a)** 3.8, **(b)** 4.5, **(c)** 4.9, and **(d)** 5.3 eV.

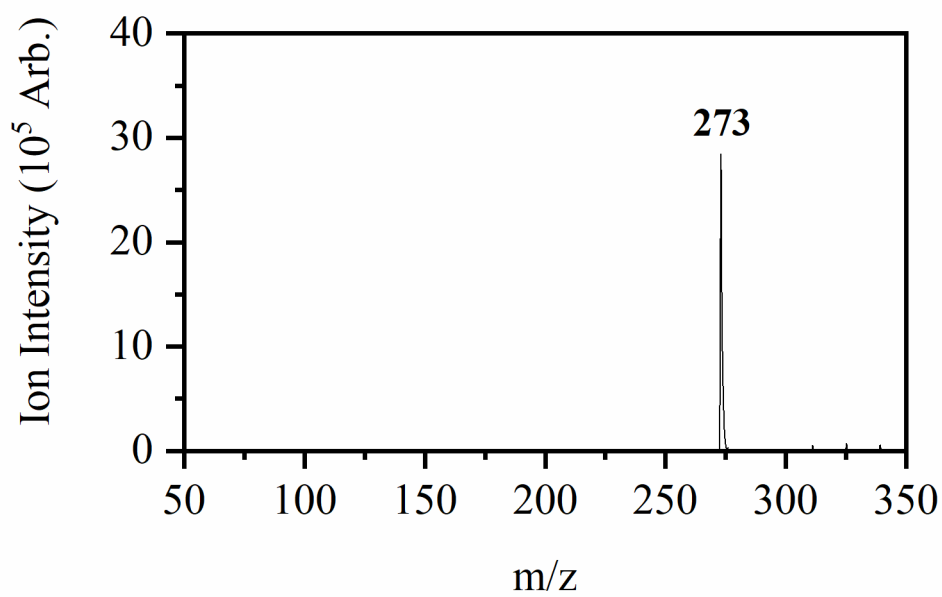
435 **Figure 4. (a)** Gas-phase UV absorption (photodepletion) spectrum of [PBSA-H]<sup>-</sup>. **(b-**  
436 **d)** Photofragment production spectra of the three photofragments with m/z 80, 193, and 208,  
437 respectively. The solid line is a five-point adjacent average of the data points.

438 **Figure 5.** Relative ion yield plots for the m/z 80, 193, and 208 photofragments of [PBSA-H]<sup>-</sup>  
439 between 3.25-5.25 eV.

440 **Figure 6.** Parent ion dissociation curve of [PBSA-H]<sup>-</sup> along with production curves for the  
441 three most intense fragments formed upon HCD between 0-75% energy. The curved lines  
442 included with the data points are a five-point adjacent average of such points and are provided  
443 as a viewing guide, to emphasize the profile for each individual fragment.

444

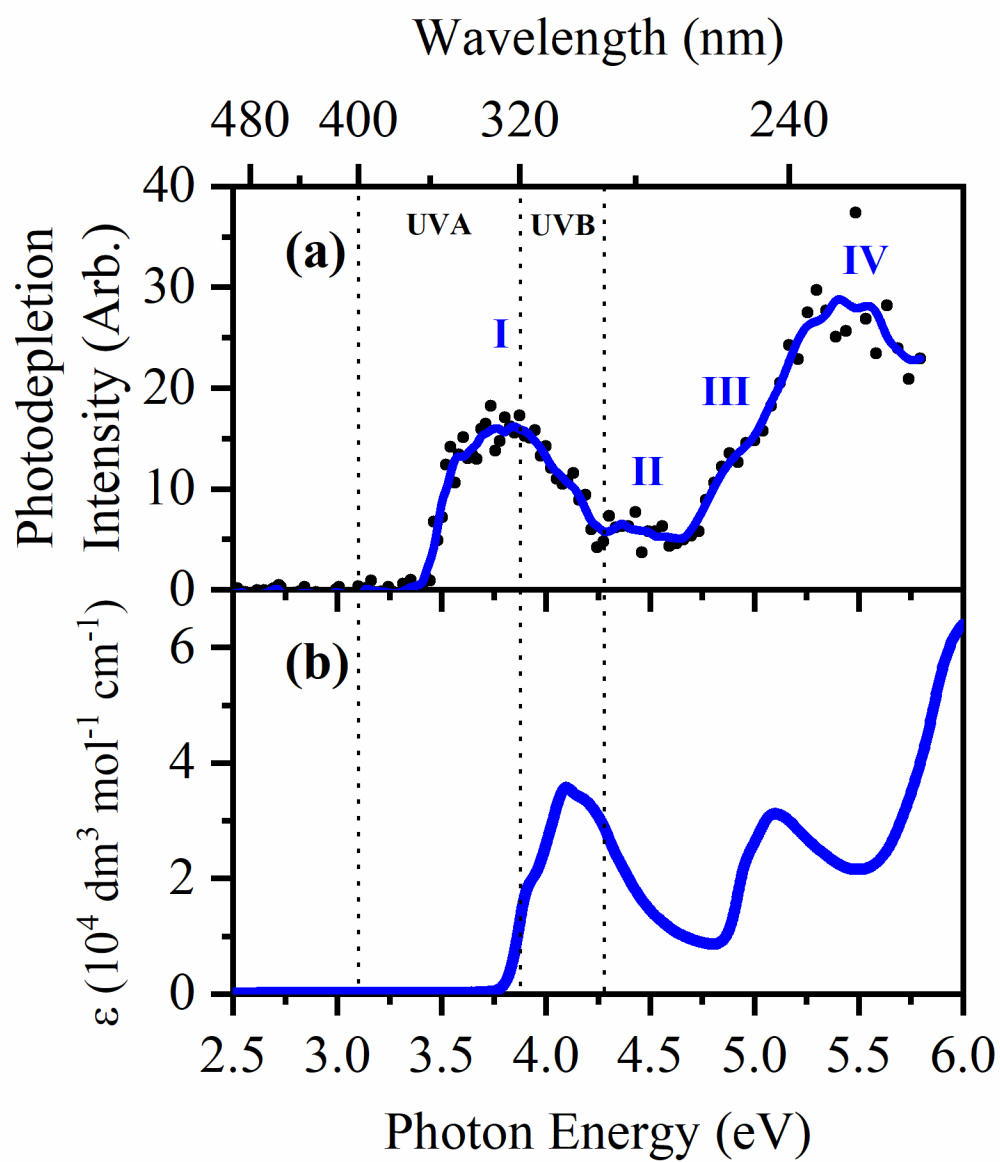
445



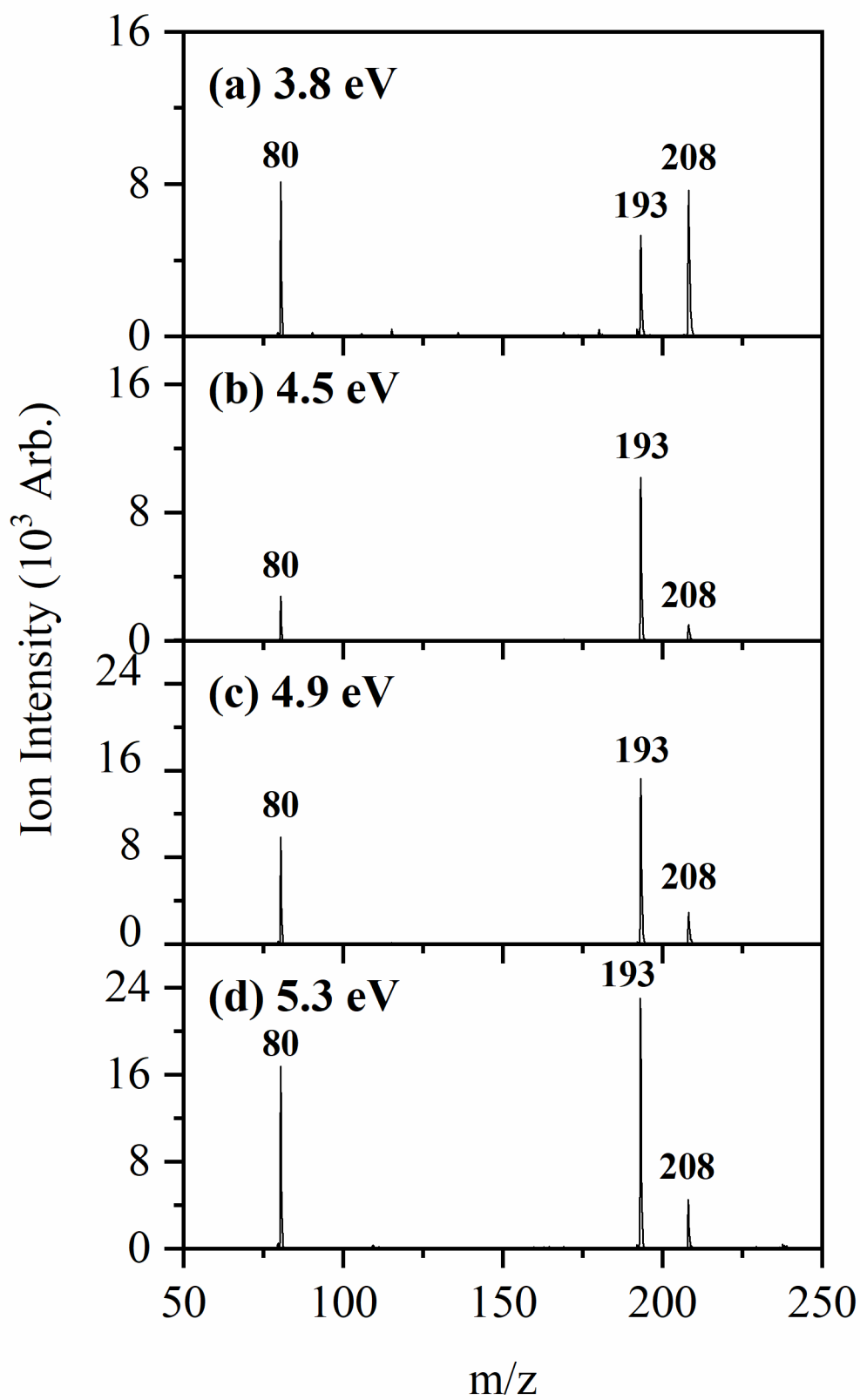
447

448 **Figure 1.**

449

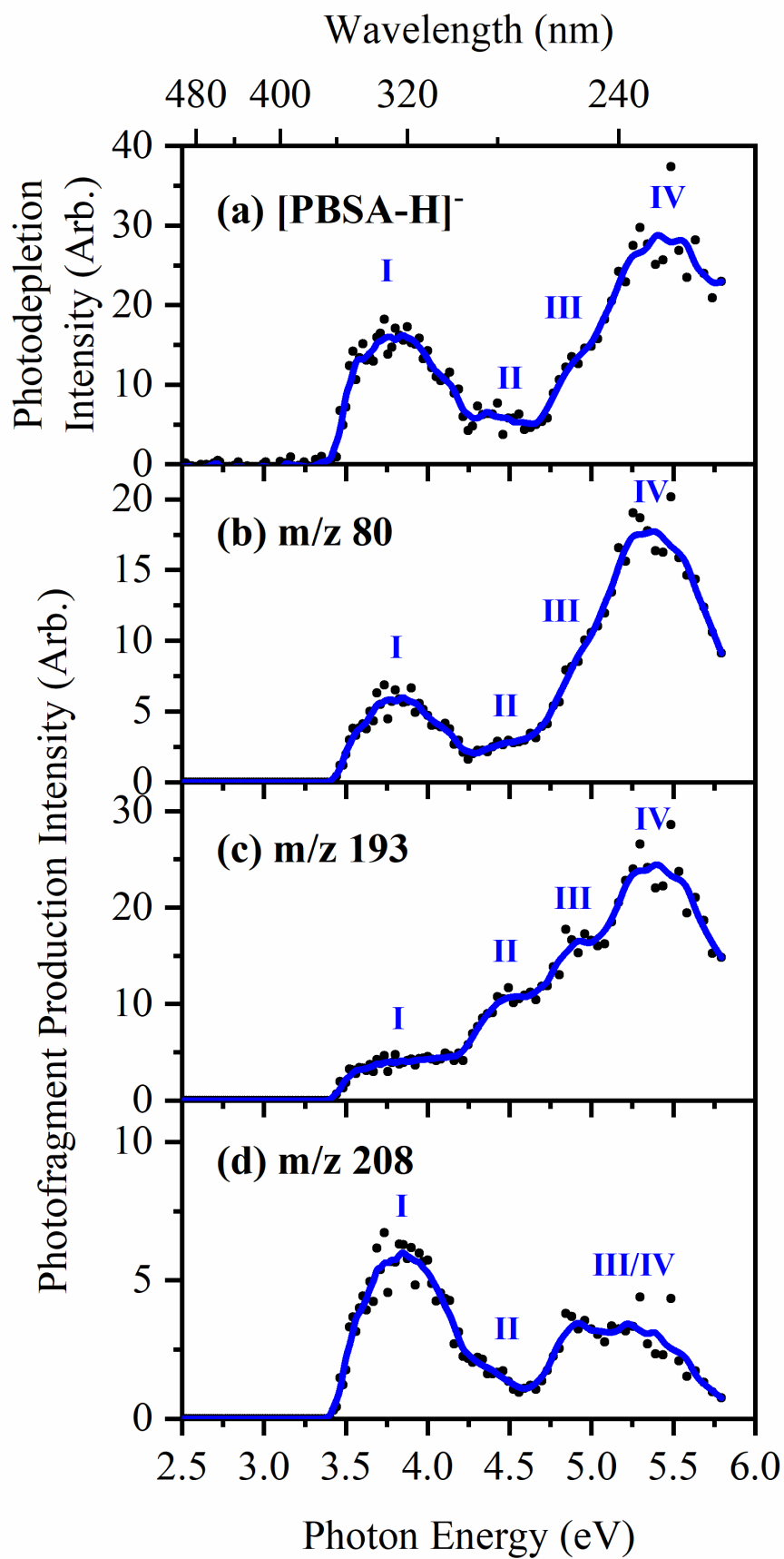


450  
 451 **Figure 2.**  
 452



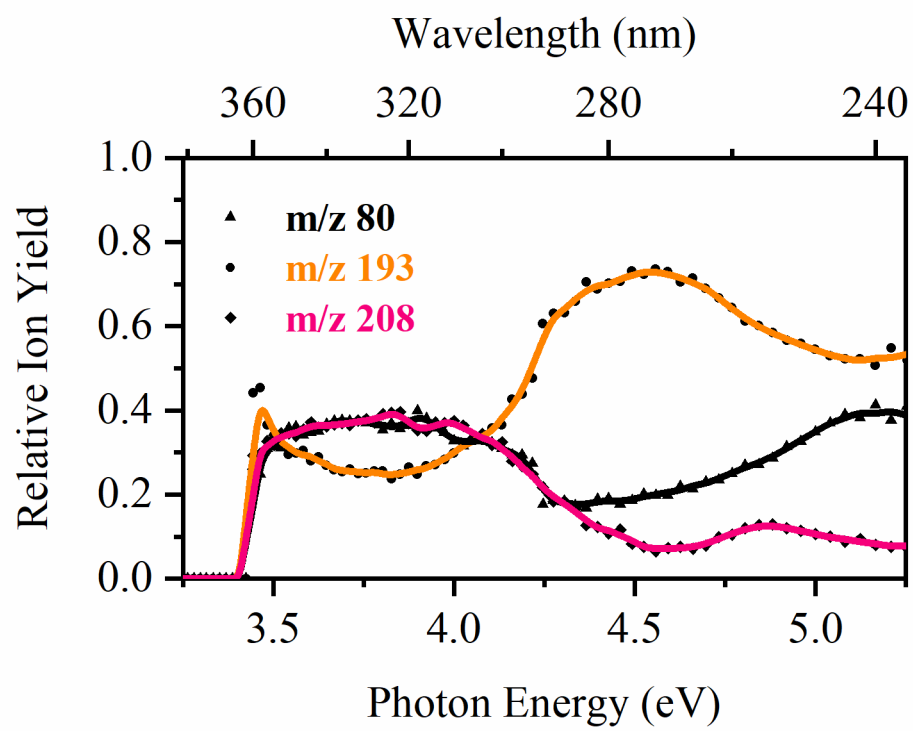
453  
454  
455

**Figure 3.**



456

457 **Figure 4.**

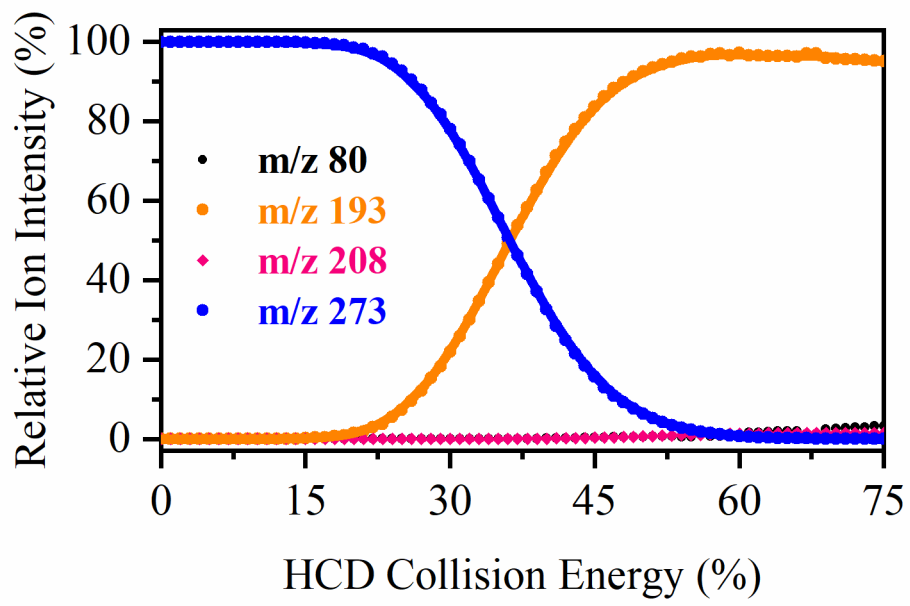


458

459 **Figure 5.**

460

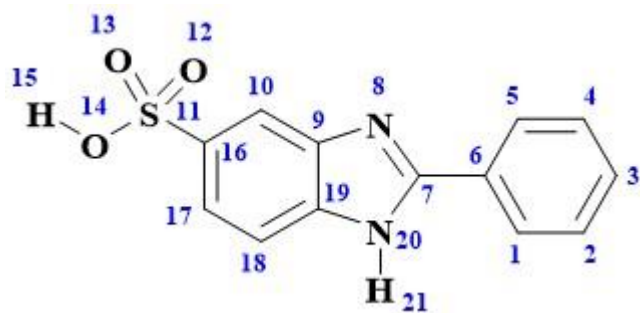
461



462

463 **Figure 6.**

464



465

466

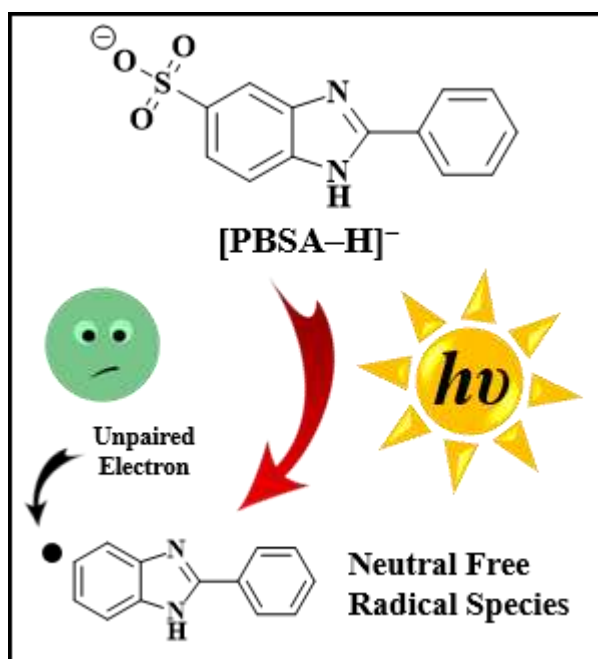
467 **Scheme 1.**

468

469 **TOC GRAPHICAL ABSTRACT**

470 2-phenylbenzimidazole-5-sulfonic acid (PBSA) is a common UV filter, which is known to  
471 exhibit photosensitizing properties. Using novel laser-interfaced mass spectrometry, we  
472 directly identify the UV photodegradation products of PBSA, and present evidence that the T<sub>1</sub>  
473 state, associated with photosensitization, decays with direct free radical production.

474



475

476

477

478 **Supporting Information**

479

480 **Direct Observation of Photochemical Free Radical Production from the Sunscreen 2-**  
481 **Phenylbenzimidazole-5-Sulfonic Acid via Laser-Interfaced Mass Spectrometry**

482

483 Natalie G. K. Wong, Jacob A. Berenbeim and Caroline E. H. Dessent\*

484 Department of Chemistry, University of York, Heslington, York, YO10 5DD, U.K.

485

486 \* Corresponding author: Email: [caroline.dessent@york.ac.uk](mailto:caroline.dessent@york.ac.uk)

487

488

489

490 S1. Laser Power Measurements

491 S2. Electron Detachment Action Spectra

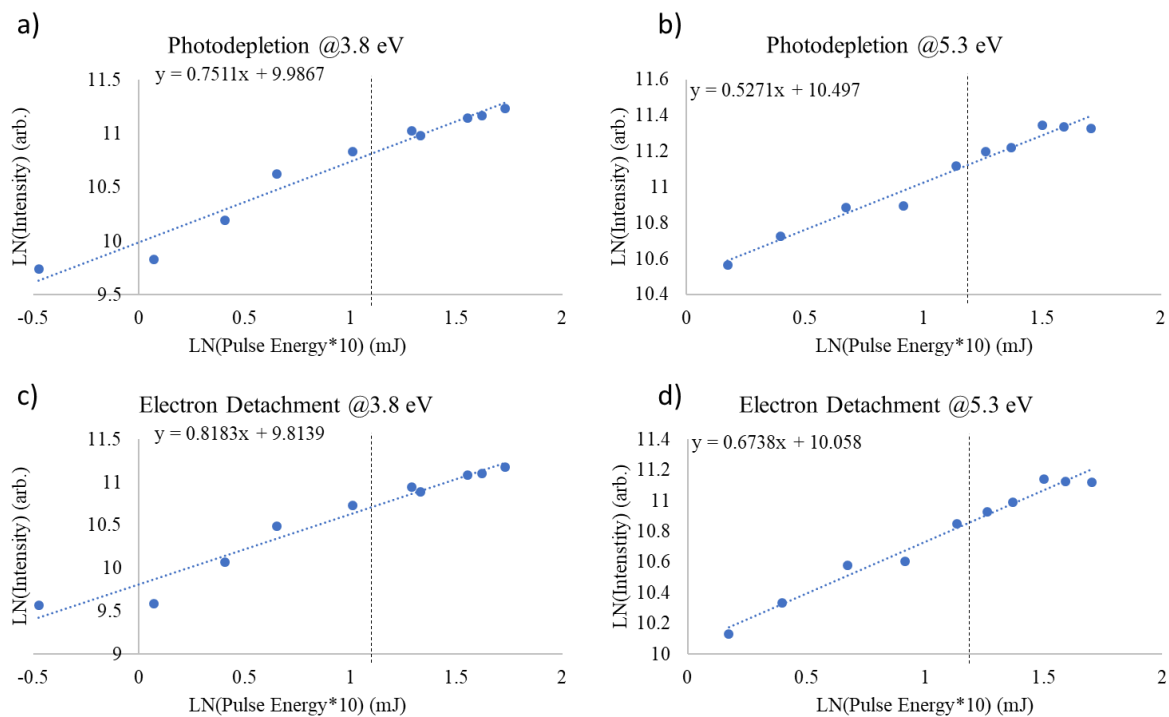
492

493 **Section S1: Laser Power Measurements**

494 Laser power measurements were conducted on [PBSA-H]<sup>-</sup> at two photon energies, 3.8 and 5.3  
495 eV, to test for the presence of multiphoton effects. The plots displayed in Figures S1-S2 include  
496 measurements of the power dependence of photodepletion, electron detachment (see Section  
497 S2), and the m/z 80, 193 and 208 photofragments.

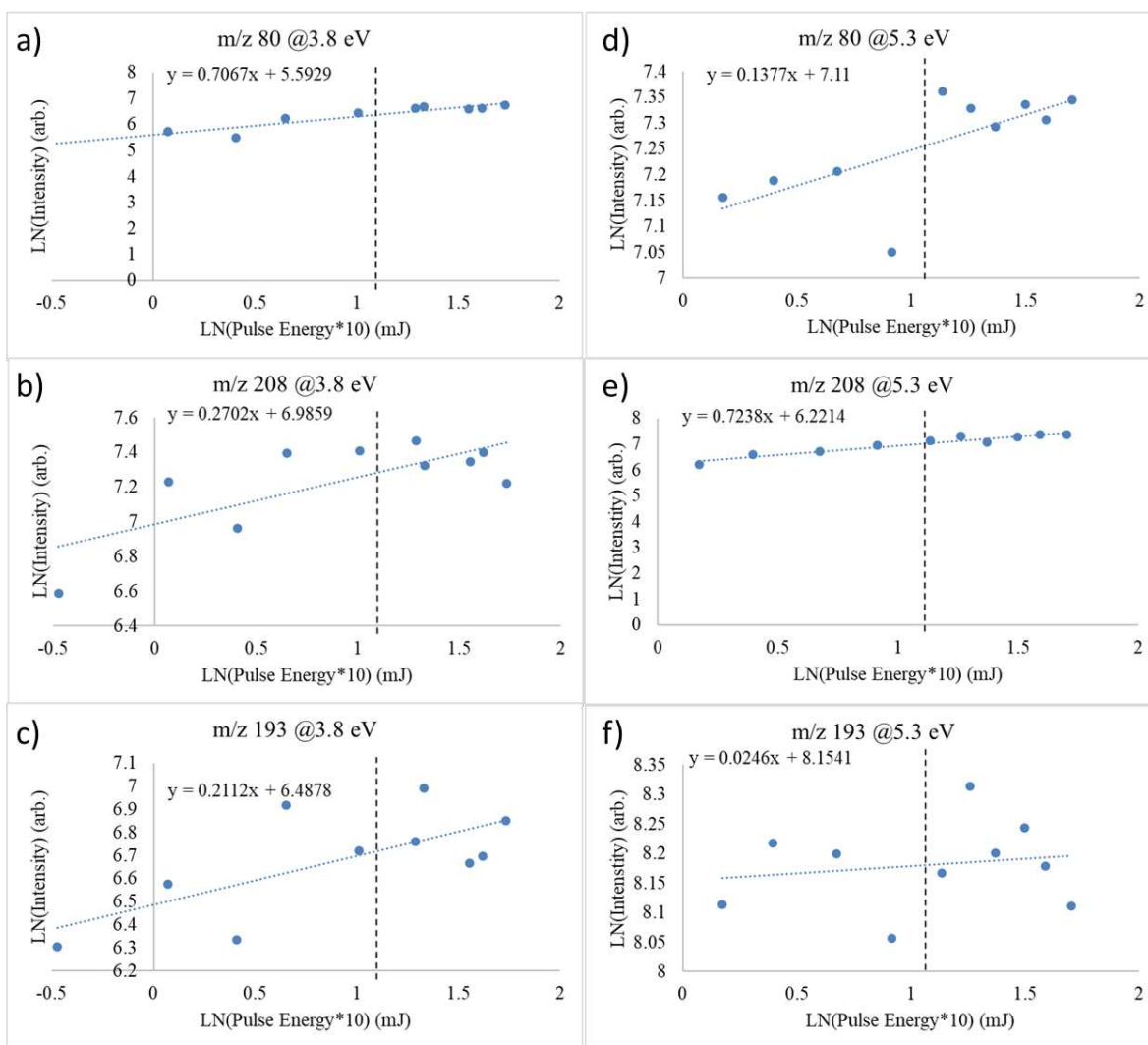
498  
499 The ln-ln of the data has been plotted and overlain with a pseudolinear fit. The resultant slope  
500 is proportional to the number of absorbed photons.<sup>1</sup> The slopes at both photon energies measure  
501 less than 1 (see Figures S1-S2 for values). This result indicates that the action response is not  
502 multiphoton in nature. Additionally, the pseudolinear slope is less than one over the fitted  
503 region and likely indicates saturation of the linear transition.

504



505  
 506  
 507  
 508  
 509

**Figure S1 Power Dependence Spectra** of photodepletion signal at a) 3.8 eV and b) 5.3 eV and of photoelectron signal at c) 3.8 eV and d) 5.3 eV. Vertical lines indicate pulse energies used during the experiment.



510

511

512 **Figure S2 Power Dependence Spectra** of ion photofragments m/z 80, m/z 208, and m/z 193  
 513 at a-c) 3.8 eV and d-f) 5.3 eV. Vertical lines indicate pulse energies used during the experiment.

514

## 515 Section S2: Electron Detachment Action Spectra

516 The electron detachment yield of [PBSA-H]<sup>-</sup> is given in Figure S3. The electron loss is not  
517 directly measurable within our instrument, thus these spectra are calculated assuming that any  
518 depleted ions that are not detected as ionic photofragments are, instead, losing an electron, i.e.  
519 the electron detachment yield = photodepletion ion count –  $\Sigma$  photofragment ion counts. This  
520 assumes that both the parent ions and photofragments are detected equally in the mass  
521 spectrometer, a reasonable assumption for the systems studied here where the parent ions and  
522 fragment ions are reasonably close in m/z.

523 Compared with the photodepletion spectrum displayed in the main text (Figure 2a), the electron  
524 detachment yield curve displays a similar profile, indicating that the electron detachment is the  
525 main photodepletion pathway. (Note that we have not adjusted the scans presented in Figure  
526 S3 by  $\lambda$  (see experimental section), whereas the spectrum in Figure 2a of the main text are.  
527 Due to this, the spectral intensity in the higher energy region is moderately reduced in the  
528 spectra displayed in Figure S3.)

529 As discussed in the main text, our calculations indicate that the vertical detachment energy of  
530 [PBSA-H]<sup>-</sup> is ~4.4 eV. From the electron detachment yield spectrum shown in Figure S3, this  
531 suggests that electrons are being detached below the VDE for [PBSA-H]<sup>-</sup>. We have seen  
532 similar effects in deprotonated adenosine monophosphate anions,<sup>[1]</sup> and this observation  
533 suggests that upon electronic excitation, the excess electron has access to a pathway that allows  
534 it to detach at energies below the VDE.

535 To give some further information about the relative extent of electron detachment versus ionic  
536 fragmentation, Table S1 provides ion counts measured in a typical experimental run conducted  
537 in this work. These numbers again show that electron detachment is the major excited state  
538 decay channel for gaseous [PBSA-H]<sup>-</sup> is electron detachment.

539 [1] R. Cercola, E. Matthews, C. E. H. Dessent, *J. Phys. Chem. B* **2017**, *121*, 5553–5561.

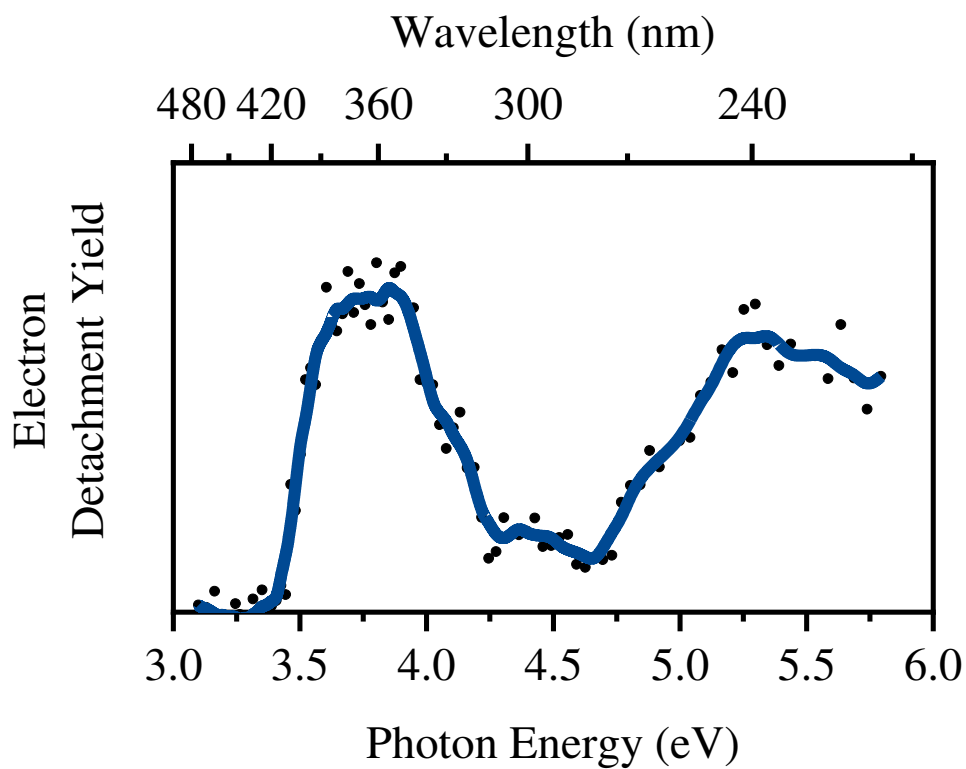
540 **Table S1** Percent electron depletion of [PBSA-H]<sup>-</sup> calculated directly from precursor ion and  
541 ionic photofragment intensities.

		Intensity (ion counts)		
Ion		3.8 eV	4.36 eV	5.5 eV
Precursor	Ion			
Depletion		215362	63784	213055
m/z 80		8105	2150	11960
m/z 193		5298	7946	17991
m/z 208		7665	1586	1598
% electron detachment		90.2	81.7	85.2

542

543

544



545  
546  
547  
548  
549  
550

**Figure S3** Electron detachment yield of [PBSA-H]<sup>-</sup>. The solid blue lines are five-point adjacent averages of the data points.